Lattice Boltzmann simulation of droplet dynamics on granular surfaces with variable wettability

Hengyi Kang and Sérgio D. N. Lourenço*
Department of Civil Engineering, The University of Hong Kong, Pokfulam, Hong Kong SAR, People's Republic of China

W. M. Yan
Department of Civil and Environmental Engineering, The University of Auckland, Auckland 1010, New Zealand

(Received 12 September 2017; revised manuscript received 4 May 2018; published 16 July 2018)

Soil-composing particles undergo wettability changes, impacting hydraulic and mechanical processes such as erosion and landslides. Such processes evolve at very small scales, typically at the particle level. Here we capture the evolution of liquid interfaces in a single particle and several particles with the lattice Boltzmann (LB) method. The paper presents a three-dimensional LB study on the droplet dynamics on a layer of uniformly packed spherical particles with varying size and intrinsic contact angle (CA) aimed at mimicking conditions comparable to those of real soils. The numerical droplet is initialized close to the granular surface and deposited by gravity. Three spreading and infiltration behaviors were identified: a droplet with a stable apparent CA, a droplet with a metastable apparent CA before infiltration, and immediate infiltration. The results showed that the formation of a droplet with a stable or metastable spherical-cap shape depends on the particle size and the intrinsic CA. Furthermore, the initial wetted zone expansion was found to be governed by inertial effects with its behavior characterized by a power law. Finally, the apparent CA, which is closely related to the intrinsic CA, was found to be influenced by the particle size due to a significant portion of the droplet being embedded into the granular surface for the larger particles and reducing the apparent CA. This paper provides a basis for future research targeting the behavior of droplet interaction with granular surfaces with variable intrinsic CAs (from wettable to superhydrophobic) such as soils and other granular materials for industrial applications. The numerical approach implemented can also be extended to model other dynamic processes for a droplet, such as evaporation, high-velocity impacting, and lateral sliding.

DOI: 10.1103/PhysRevE.98.012902

I. INTRODUCTION

Droplet dynamics, such as spreading, infiltration, or standing with a spherical cap, on granular surfaces widely occurs in nature. In soil science, water droplet infiltration is vital for crop irrigation and productivity [1,2]. In earth surface processes, the impact of water drops in the soil leads to splash erosion [3], while in wildfire-affected slopes soil water repellency inhibits infiltration with the water drops rolling on the surface and generating rill erosion [4]. Its effects have also been studied and mimicked by various disciplines with an economic intent; examples include textiles [5], powder technology [6], ink jetting [7], and new smart materials [8]. By using an advanced numerical tool that can capture the evolution of liquid interfaces in a single particle or several particles, this paper provides insight into droplet interaction and dynamics with granular surfaces.

Interaction of droplets with porous media depends on the morphology and surface wettability of the substrate. For granular materials such as soils, morphology refers to the size and shape of the particles and how they are arranged to form a surface with voids [9]. Wettability refers to the adhesive or repulsive effects between a liquid and a particle surface. Under different configurations of particle size and wettability, the interplay between these physical characteristics will dictate whether a droplet sits on the surface, infiltrates slowly, or infiltrates quickly. Placing a droplet onto a permeable surface leads to an intricate solid-fluid interaction due to the interplay between the droplet infiltration and spreading (Fig. 1). The droplet may reach a stable configuration with the particles, standing still above the porous surface. It may get slowly absorbed but can still recoil to form a spherical cap. If the infiltration is rapid enough, the droplet can remain unstable with a distorted shape before infiltration [10].

The interaction behavior and dynamics of a droplet with a surface are strongly linked to the surface wettability. The interaction diverges between a rough and porous surface and a flat and smooth surface. For a flat surface, the intersection angle between the droplet interface and the surface can be measured as a direct expression of wettability, which is defined by the contact angle (CA). For a granular surface, Fig. 2(a) shows that CAs at two different length scales are present. The CA on a particle surface is the intrinsic CA, while that on a surface made of many particles is the apparent CA.

The apparent CA is measured directly on a granular surface with the sessile drop method (SDM), which is widely used in solid surfaces and granular solids in material science [11] and soil science [12]. The SDM procedure consists of sprinkling particles on a double-sided tape attached to a microscope glass slide as the base. A sessile drop is released from a syringe close to the particle layer. The gap between the droplet and

*lourenco@hku.hk

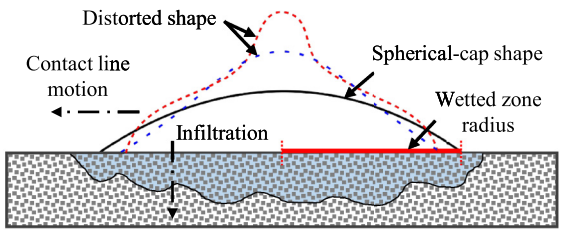

FIG. 1. Sketch of droplet interaction with porous surface.

the tested surface is reduced to eliminate the impacting effect and prevent splashing of the droplet. During the subsequent process, a sequence of side images is captured by a video camera. If a droplet gets slowly absorbed into the granular surface, the apparent CA shall be measured at the first frame when the droplet displays a spherical-cap shape. For a droplet eventually standing above the surface, the reading can be taken after the oscillation stops. Figure 2(b) shows a side photograph of the SDM setup, where the apparent CA is measured for a water droplet sitting statically on a layer of hydrophobic glass beads. Essentially, it is the intrinsic CA that governs the bonding capillary forces [13], the liquid morphology [14], the soil water retention [15], and capillary imbibition [16] in a partially saturated soil. Yet, only the apparent CA on a layer of particles can be measured. Therefore, inferring the intrinsic CA from the apparent CA is of high importance.

The simplest approach to derive the apparent CA on rough solid surfaces assumes the crevices filled with water or entrapped by air, as postulated by the Wenzel model [17] and Cassie-Baxter model [18], respectively. The Wenzel model predicts an apparent CA smaller than the intrinsic CA since the surface roughness increases the contact area between the liquid

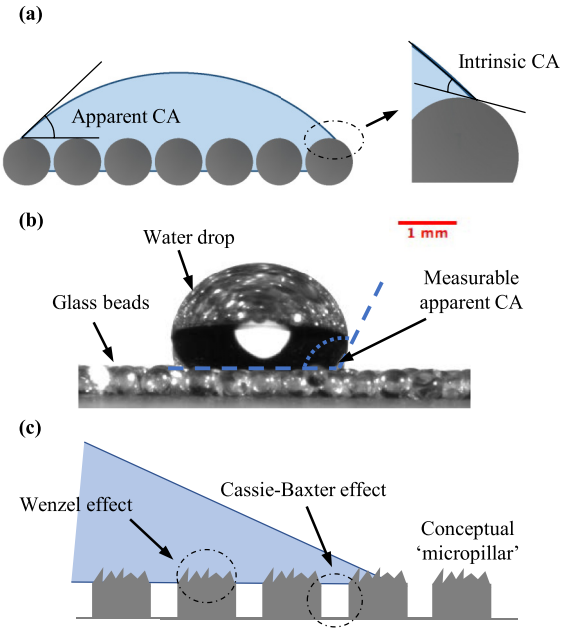

FIG. 2. (a) Sketch of intrinsic CA and apparent CA on a particle layer. (b) Image of the SDM test, showing a 10-μL water drop standing above a layer of hydrophobic glass beads. (c) Illustration of the Bachmann-McHale model.

and the solid. In contrast, the Cassie-Baxter model predicts a larger apparent CA since a greater fraction of the liquid is in contact with the immiscible air phase. However, reality lies between the two idealized cases. Figure 2(c) illustrates an intertwined model involving both the Wenzel and Cassie-Baxter effects developed by Bachmann and McHale [19]. The model assumes the droplet to arch over the adjacent particles (Cassie-Baxter effect) while the wetted surface area at each particle is larger than its projection area (Wenzel effect). If the particle shape is simplified as spherical, the wetted surface area can be determined with a known intrinsic CA. The model was adopted to interpret the apparent CA on glass beads and sands. Nevertheless, the three models were derived by advancing the droplet interface to the adjacent micropillar, and the change in surface free energy is zero if the apparent CA is at its equilibrium value. This requires the assumption of an infinitesimal roughness scale compared to the droplet, where the volume of the liquid embedded into the porous media is negligible. However, a porous surface may be composed of particles with sizes comparable to the droplets. Previous experimental studies found that the apparent CA was influenced by the particle size but the results are contradictory [20–22]. These challenges cannot be clarified with size-independent models.

Spreading dynamics has been numerically studied by two different approaches. One approach is the lubrication-theory-based models treating the porous media as a continuum [23–27]. A spherical-cap or parabolic shape with no inertial effects is assumed for a droplet with a prescribed apparent CA while imbibition into the porous medium is described by the Darcys flow [25]. The method is limited to modeling the contact line motion, mostly for the media with small pores where the details of the pore-scale morphology are not considered. However, the assumption of a pure viscous spreading decoupled from inertia may not hold true for a real droplet with prominent infiltration and oscillation. Neither can it be used to study the effect of the intrinsic CA on the droplet behaviors and the apparent CA. An alternative approach is to conduct a pore-scale simulation [28–33]. The topography of a porous medium defining the spatial distribution of solids and voids with a pore-scale resolution is required as the computational domain for solving the multiphase Navier-Stokes equations. Though the direct numerical simulation is computationally expensive requiring parallel implementation of the algorithm in supercomputers, it provides the distribution of the liquid phase inside and outside the porous media. Both the information of a droplet spreading above the surface and the microscopic insights into the flows in pores can be retrieved. Therefore, it serves as a tool to investigate the effects of the pore-scale morphology and wettability on droplet dynamics.

Droplet dynamics has been investigated by pore-scale simulations. Hyväluoma *et al.* [29] simulated the droplet infiltration into a porous matrix reconstructed from scanned microtomographic images of paper fibers. Both the volume above the surface and the preferential flow infiltration were monitored. Frank *et al.* [30,33] explored the evolution of the wetted zone radius and droplet height decreasing on arrays of capillary tubes with different shapes, intrinsic CAs, and pore fractions. They found that the power law describing the initial wetted zone growth on flat surfaces [34] can also be extended

to a porous surface. The droplet displayed the spherical-cap shape, which is essential for the measurement of the apparent CA. An advantage of the pore-scale method is its ability to capture rapid infiltration in wettable porous surfaces. Ding and Theofanous [31] investigated the fast infiltration of droplets into capillary tubes. The downward pore flow was so rapid that the liquid phase in the tubes ruptured from the droplet. Similarly, Taghilou and Rahimian [32] simulated the droplet infiltration into two-dimensional porous media consisting of sparsely randomly distributed solid nodes. Since the infiltration was fast, the droplets were distorted and no apparent CA was exhibited. Despite the above studies, the formation mechanism of droplets with a spherical-cap shape and its dependence on the properties of the porous media remain unclear. Moreover, the substrate geometry in the above studies differs from those of granular materials, which is the focus of our research.

The present paper provides direct pore-scale insight into the interaction and dynamics of droplets with a layer of spheres. It uses grains that match those of medium-sized sands, which are a very common geological material all over the world. Likewise, the droplet size is within the range of natural rainfall drops [35]. The numerical setup is physically based on the experimental setup of the SDM test. While the commonly available SDM apparatus only records the droplet spreading above the granular surface with 83 frames per second [36], the lattice Boltzmann (LB) simulation captures the distribution of the liquid phase inside and outside the particle layer, with a much higher temporal resolution, which for this paper was in the range of a few microseconds. The apparent CA and the evolution of the droplet shape can be precisely measured, together with the pore-scale flow dynamics during infiltration. By conducting simulations under different configurations of particle size and intrinsic CA, the specific objectives are (1) to identify the various modes of droplet dynamics, (2) to explore the temporal evolution of the wetted zone radius to study the lateral propagation of the droplet contact lines, and (3) to investigate the linkage between the apparent CA and the intrinsic CA.

II. NUMERICAL METHOD

The pore-scale numerical simulations of droplet dynamics on a layer of particles involves dealing with the movement of air-water interfaces on porous surfaces with variable wettability. Such problems can be handled with various multiphase LB methods (e.g., pseudopotential LB methods [37,38], free-energy models [39–41], and phase-field LB method [42,43]). The LB method, originally generated from gas kinematics, is known for the efficient parallelization of the algorithm and flexibility in dealing with irregular boundaries [44]. Therefore, multiphase LB methods have been widely applied in simulating pore-scale flows, such as unsaturated permeability [45], wetting-drying in porous media [46], capillary rise [47], Pickering emulsion [48], and colloid hydrodynamics [49].

In the present paper, the simulation is performed with the phase-field LB method [43]. The system of binary fluids adopts the one-fluid formulation where a phase index field C is defined to describe the phase that occupies each computational cell. The phase index C is around one for the liquid phase and is around zero for the gas phase. The value gradually changes from zero to one in the interface. The evolution of the phase field is governed by the minimization of the free energy given by

$$\Psi = \Psi_b + \Psi_s = \int_V \left[E_0(C) + \frac{\kappa}{2}|\nabla C|^2 \right] dV + \int_S (\phi_0 - \phi_1 C_s + \phi_2 C_s^2 - \phi_3 C_s^3 + \dots) dS, \quad (1)$$

where Ψ is the total free energy, and the subscripts b and s mean the contributions from the bulk fluids and the solid boundaries. There are two terms within the Ψ_b, the local bulk energy $E_0 = \beta C^2(C-1)^2$ and the interface-induced energy $\frac{\kappa}{2}|\nabla C|^2$. The constants β and κ can be related to the surface tension σ and interface thickness ξ by

$$\sigma = \frac{\sqrt{2\kappa\beta}}{6}, \quad (2)$$

$$\kappa = \frac{\beta\xi^2}{8}. \quad (3)$$

Ψ_s is nonzero only for the fluid nodes adjacent to the solid nodes, C_s is the composition at a solid surface, and the ϕ_s are the constant coefficients.

Minimizing the bulk free energy Ψ_b for the fluid phase leads to the Cahn-Hilliard (CH) equation:

$$\frac{\partial C}{\partial t} + \nabla \cdot (\boldsymbol{u} C) = M \nabla^2 \mu, \quad (4)$$

where $\boldsymbol{u}$ is the velocity, μ is the chemical potential, and M is the mobility, a numerical parameter controlling the rate of diffusion. The chemical potential is derived from the free energy:

$$\mu = \mu_0 - \kappa \nabla^2 C = \frac{\partial E_0}{\partial C} - \kappa \nabla^2 C. \quad (5)$$

The μ_0 is called the local part of the chemical potential, and the $-\kappa\nabla^2 C$ is the interface-induced chemical potential. Since E_0 takes the form of the double-well potential function, C will be close to either zero or one in the pure single-phase region. The negative sign in the nonlocal term $-\kappa\nabla^2 C$ helps build a stable diffusive gas-liquid interface. The two competing terms mean that the phase index C is stable either completely separated as the pure single phase or well mixed as the interface. Therefore, the evolution of the CH equation results in the phase separation while the total free energy in the system is decreasing.

For the fluid nodes adjacent to the solid surface, minimizing the $\Psi_b + \Psi_s$ leads to a partially wetting boundary condition where the CA can be defined at the fluid-solid interface by specifying the gradient of C [50]. The boundary condition is established as

$$\boldsymbol{n} \cdot \nabla C|_s = -\cos\theta^{\mathrm{eq}} \sqrt{\frac{2\beta}{\kappa}} (C_s - C_s^2), \quad (6)$$

where θ^{eq} is the equilibrium CA at the solid surface.

Solving the CH equation provides the spatial distributions of density ρ, the kinematic viscosity ν, and the surface tension force $\boldsymbol{F}_s$. Here, density and viscosity are both the necessary material properties for solving the incompressible NS equation. They can be calculated from the index C simply

through linear mapping, and are written as

$$\rho = C\rho_l + (1-C)\rho_g, \tag{7}$$

$$\frac{1}{\nu} = \frac{C}{\nu_l} + \frac{1-C}{\nu_g}, \tag{8}$$

where the subscripts l and g indicate the liquid phase and the gas phase. The surface tension force $\boldsymbol{F_s}$ applied at the interfacial region is proportional to the gradient of the interface-induced chemical potential, given by

$$\boldsymbol{F_s} = \kappa C \nabla \nabla^2 C. \tag{9}$$

The formulation based on the chemical potential is called the potential form [42]. Together with the standard isotropic spatial discretion, the nonphysical velocities at the interfacial region in the multiphase LB method (also termed as spurious currents) can be minimized [51].

With the information provided by the CH equation, the LB method computes the evolution of the mesoscale particle probability functions, from which the macroscale velocity and pressure are obtained. The standard discrete Boltzmann equation (DBE) with the body force term for macroscopic motion of fluid flows is

$$\frac{\partial f_\alpha}{\partial t} + \boldsymbol{e_\alpha}\cdot\nabla f_\alpha = -\frac{1}{\lambda}\left(f_\alpha - f_\alpha^{\mathrm{eq}}\right) + \frac{1}{c_s^2}(\boldsymbol{e_\alpha}-\boldsymbol{u})\cdot\boldsymbol{F}\Gamma_\alpha(\boldsymbol{u}). \tag{10}$$

Here, f_α is the distribution function, $\boldsymbol{e_\alpha}$ is the discrete velocity for the direction α, c_s is the lattice speed of sound, and λ is the relaxation time which is related to the kinematic viscosity by $\nu = \lambda c_s^2$. $\boldsymbol{F}$ is the body force term $\boldsymbol{F} = \boldsymbol{F_s} + \rho\boldsymbol{g}$, including the contributions from surface tension force and gravity. $\Gamma_\alpha(\boldsymbol{u}) = f_\alpha^{\mathrm{eq}}/\rho$, and f_α^{eq} is the equilibrium distribution function defined by

$$f_\alpha^{\mathrm{eq}} = t_\alpha \rho\left[1 + \frac{(\boldsymbol{e_\alpha}\cdot\boldsymbol{u})}{c_s^2} + \frac{(\boldsymbol{e_\alpha}\cdot\boldsymbol{u})^2}{2c_s^4} - \frac{(\boldsymbol{u}\cdot\boldsymbol{u})}{2c_s^2}\right], \tag{11}$$

where t_α is the weight for the direction α.

The LB formulation has been proved to be equivalent to the artificial compression method in solving the incompressible Navier-Stokes (NS) equation by the Chapman-Enskog analysis [52]. However, the original formulation stores the base density with the hydrodynamic pressure as a small perturbation in the distribution functions and only applies to the multiphase problem with nonuniform density field. The problem is solved by defining a new distribution function $g_\alpha = f_\alpha c_s^2 + (p - \rho c_s^2)\Gamma_\alpha(0)$ to split the density [38]. Similarly, the g_α^{eq} is transformed as $g_\alpha^{\mathrm{eq}} = f_\alpha^{\mathrm{eq}} c_s^2 + (p-\rho c_s^2)\Gamma_\alpha(0)$. The DBE for the new distribution function is

$$\begin{aligned}\frac{\partial g_\alpha}{\partial t} &+ \boldsymbol{e_\alpha}\cdot\nabla g_\alpha \\ &= -\frac{1}{\lambda}\left(g_\alpha - g_\alpha^{\mathrm{eq}}\right) + (\boldsymbol{e_\alpha}-\boldsymbol{u})\cdot\left\{\nabla\rho c_s^2[\Gamma_\alpha(\boldsymbol{u}) - \Gamma_\alpha(0)]\right. \\ &\quad \left. + \boldsymbol{F}\Gamma_\alpha(\boldsymbol{u})\right\},\end{aligned} \tag{12}$$

from which the evolution of pressure and velocity in the macroscopic NS equations can be recovered as

$$\frac{\partial p}{\partial t} + \rho c_s^2 \nabla\cdot\boldsymbol{u} = 0, \tag{13}$$

$$\rho\left(\frac{\partial \boldsymbol{u}}{\partial t} + \boldsymbol{u}\cdot\nabla\boldsymbol{u}\right) = -\nabla p + \boldsymbol{F} + \nabla\cdot\left\{\rho c_s^2\lambda[\nabla\boldsymbol{u} + (\nabla\boldsymbol{u})^T]\right\}. \tag{14}$$

By integrating the DBE with a trapezoidal approximation over a small time step δt [43], the lattice Boltzmann equation for numerical implementation is

$$\begin{aligned}&\overline{g}_\alpha(\boldsymbol{x},t) - \overline{g}_\alpha(\boldsymbol{x}-\boldsymbol{e_\alpha}\delta t, t-\delta t) \\ &= -\frac{1}{\tau+1/2}(\overline{g}_\alpha - \overline{g}_\alpha^{\mathrm{eq}})|_{(\boldsymbol{x}-\boldsymbol{e_\alpha}\delta t, t-\delta t)} \\ &\quad + \delta t(\boldsymbol{e_\alpha}-\boldsymbol{u})\cdot(\kappa C\nabla\nabla^2 C + \rho\boldsymbol{g})\Gamma_\alpha(\boldsymbol{u}) \\ &\quad + \delta t(\boldsymbol{e_\alpha}-\boldsymbol{u})\cdot\nabla\rho c_s^2[\Gamma_\alpha(\boldsymbol{u}) - \Gamma_\alpha(0)],\end{aligned} \tag{15}$$

where $\tau = \lambda/\delta t$. With the temporal discretion, the truncation error is $O(\Delta t^2)$. The velocity and the macroscopic pressure are obtained from the distribution functions by

$$\rho\boldsymbol{u} = \sum_\alpha \boldsymbol{e_\alpha}\overline{g}_\alpha + \frac{\delta t}{2}(\kappa C\nabla\nabla^2 C + \rho\boldsymbol{g}), \tag{16}$$

$$p = \sum_\alpha \overline{g}_\alpha + \frac{\delta t}{2}\boldsymbol{u}\cdot\nabla\rho c_s^2. \tag{17}$$

The same temporal discretion can also be applied to solve the CH equation [42,43]. However, the LB discretion can only recover the advection term $\nabla\cdot(\boldsymbol{u}C)$ in Eq. (4), while the nonlinear diffusion term $M\nabla^2\mu$ cannot be recovered and related to the relaxation time λ. The advantages of the LB scheme to recover both the advection term and the linear diffusion as in solving the NS equations cannot be exploited. Instead, the $M\nabla^2\mu$ shall be included as an additional term, which still relies on the finite difference approximation with first-order accuracy [53]. Therefore, the CH equation can be more efficiently solved by a full finite difference (FD) scheme [54] and then coupling with the NS equations solved by LB. We also adopt this hybrid LB-FD formulation. The advective term $\nabla\cdot(\boldsymbol{u}C)$ is discretized by a second-order group velocity control scheme. In the Cartesian coordinate system with uniform grid, the nonlinear diffusion term is approximated with the isotropic central difference scheme involving all the neighborhood nodes [55]. The third-order total variation diminishing Runge-Kutta scheme is used for the temporal discretion. For computational details for solving the CH equation, refer to computational fluid dynamics textbooks [56].

III. MODEL VALIDATION

The benchmark numerical tests on micron-scale droplet impact on flat and smooth dry surfaces in Lee and Liu [43] were replicated to validate the algorithm. The droplet spreading and recoiling dynamics is governed by the Weber number, Laplace number, and CA of the flat surface. For the 48.8-μm water droplet used in the numerical tests, the dimensionless Laplace number is $\mathrm{La} = \frac{\sigma R}{\rho_l \nu_l^2} = 1776$, which defines the relative magnitude of inertial and capillary forces to viscous forces. In terms

of the impacting velocity, the dimensionless Weber number defined as the ratio of the inertial force over the surface tension is $\mathrm{We} = \frac{\rho u^2 D_{\mathrm{drop}}}{\sigma} = 14.8$. The simulations are performed on both the hydrophilic and the hydrophobic surfaces, of which the CAs are 31 and 107°, respectively.

The numerical configuration follows Lee and Liu [43], which matches the Laplace number and the Weber number for the droplet. In LB units, the numerical box dimensions are set as $n_x = 256$, $n_y = 256$, and $n_z = 256$. The droplet diameter is set to 50, initially at the center of the domain. The liquid density is $\rho_l = 1.0$, the liquid kinematic viscosity is $\nu_l = 3.33 \times 10^{-3}$, and the surface tension is $\sigma = 7 \times 10^{-4}$. The droplet is accelerated to $u = 0.013$, followed by the collision in the normal direction to the flat surface. For the vapor phase, the density is $\rho_v = 1.188 \times 10^{-3}$ and the kinematic viscosity is $\nu_v = 0.055$. So the dynamic viscosity ratio of the numerical system is as large as 51.

Figure 3 shows the evolution of the droplet spreading diameter and the droplet height normalized by the initial droplet diameter for the surfaces with CAs of 31 and 107°. A more significant droplet bounce is observed for CA = 107° than for CA = 31°. The results agree with the numerical and experimental results in Lee and Liu [43], which demonstrates the potential of the algorithm to model the droplet dynamics on granular surfaces.

IV. NUMERICAL SETUP

The numerical setup follows that of the SDM for measuring the apparent CA by depositing a droplet on a layer of soil particles stuck to a microscope glass slide. The dimensions of the computational domain are set as $n_x = 400$, $n_y = 200$, $n_z = 400$ in LB units, and the droplet diameter is set to 96. Physically, the diameter is equivalent to 2.67 mm, which matches the 10-μL droplet commonly used in the SDM [57]. For simplicity, in the present paper, the substrate is a layer of spherical particles closely packed in a triangular pattern on the xz bottom plane (Fig. 4). The lattice nodes occupied by the particles are marked as solid nodes, implemented with the bounce-back boundary condition. The particle diameters are 24, 32, and 40, corresponding to the physical values 0.67, 0.89, and 1.15 mm, respectively. The ratios $D_{\mathrm{particle}}/D_{\mathrm{drop}}$ are 1:4, 1:3, and 1:2.4. The particle sizes are within the range of coarse sands. Intrinsic CAs on the particle surface are 30, 45, 60, 75, 90, and 105°, ranging from wettable to water repellent particle surfaces. Therefore, a total of 18 numerical tests were performed with different combinations of intrinsic CA and particle size.

In each test, the liquid density is $\rho_L = 1.0$, the liquid kinematic viscosity is $\nu_L = 3.33 \times 10^{-3}$, and the surface tension is $\sigma = 4 \times 10^{-3}$ in LB units, corresponding to $10^3\ \mathrm{kg/m^3}$, $2.34 \times 10^{-6}\ \mathrm{m^2\ s^{-1}}$, and 72.8 mN/m, respectively, in physical units. The kinematic viscosity is close to the value of 20% concentration saline water, which is 2.33 times that of pure water ($1.006 \times 10^{-6}\ \mathrm{m^2\ s^{-1}}$). Further reducing the lattice viscosity ν_L would trigger numerical instability, so a smaller physical viscosity can only be achieved by enlarging the computational domain, which would demand more computational power. Despite compromise, in terms of relative magnitude of inertial and capillary forces to viscous forces, the dimensionless Laplace number $\mathrm{La} = \frac{\sigma R}{\rho_l \nu_l^2} = 17\,280 \gg 1$ is sufficiently large so that the droplet is considered as low viscosity [58]. Such a large value has been seldom numerically investigated in the literature.

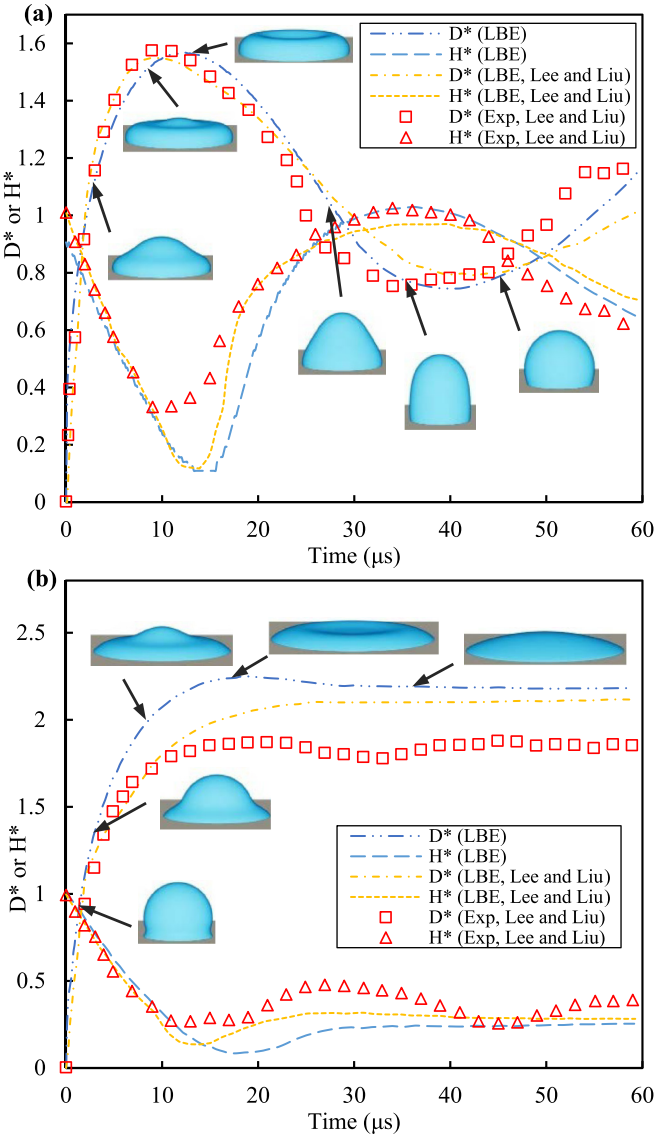

FIG. 3. Evolution of the droplet spreading diameter and the droplet height normalized by the initial droplet diameter (denoted by D^* and H^*, respectively) for a 48.8-μm droplet impacting on a flat surface with (a) CA = 107° and (b) CA = 31°.

The simulation involves a preparation stage and a gravity deposition stage. First, the droplet is initiated in a spherical

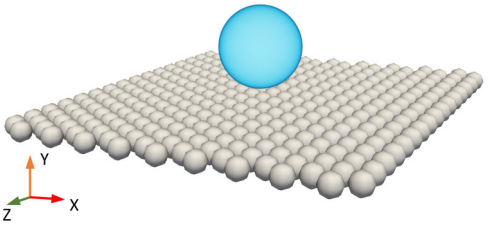

FIG. 4. Perspective view of the droplet and the particle layer. The current snapshot for illustration is for $D_{\mathrm{particle}}/D_{\mathrm{drop}} = 1:4$.

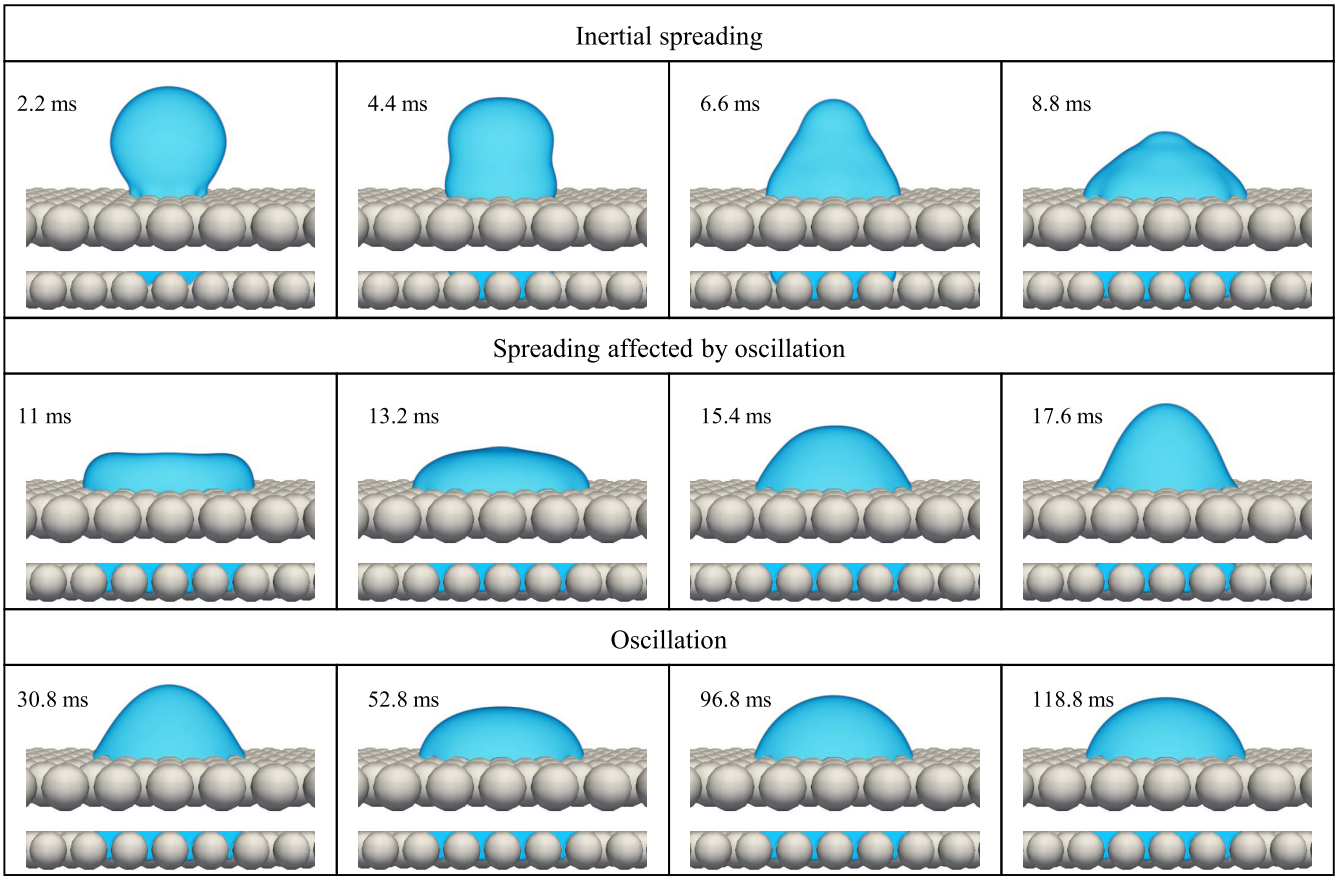

FIG. 5. Typical behavior for mode I: time sequence for test M75 with $D_{\text{particle}}/D_{\text{drop}} = 1:3$; at each time, the upper layer denotes the drop shape and contact line movement and the lower layer denotes the infiltration.

shape above the particle layer with a negligible gap. The gap is for completely separating the diffusive droplet interface with finite thickness from the granular surface. Otherwise, nonphysical mass transfer from the droplet to the granular surface will happen. The gap takes eight lattice nodes and physically this corresponds to 0.23 mm. This is similar to the SDM test, where the droplet is released near the granular surface to minimize the impacting effect. The phase index C is set as one within the droplet and is set as zero in the surrounding air. At the interface, a smooth transition is realized using a tanh function [43]. However, the distribution of the phase index C is not in an equilibrium state. The correct pressure field that fits the surface tension forces has not yet been built up. Hence, the simulation runs with no gravity until the system reaches equilibrium. Then, gravity can be applied to the liquid phase so that the droplet moves downward and touches the granular surface. The subsequent evolution process is monitored in the form of three-dimensional image files at specific time intervals. Depending on the properties of the granular surface, the computation is terminated either after the droplet fully infiltrates, or stops oscillating and stands still the surface.

The computational time required to complete the simulations with CA = 30 or 45° is approximately 48 h on a 20-core workstation with the basic OpenMP parallelism, and it takes around 96 h for CA = 60° as the infiltration is slower. The droplet cannot infiltrate for a CA starting from 75°. It takes 96 h for CA = 75° to damp out the oscillation and requires a longer period for larger CAs. Therefore, for CA = 90 and 105°, the liquid viscosity is set as a nonphysical larger value to damp out the oscillation for speeding up convergence, after the droplet finishes spreading on the surface. In this way, the simulation can be finished within reasonable computational time without affecting the equilibrium apparent CA.

V. RESULTS AND DISCUSSION

A. Droplet dynamics on granular surfaces

For clarity, a test is labeled by its particle size and the intrinsic CA. The particle layers with the diameters 0.67, 0.89, and 1.15 mm are denoted by S, M, and L, respectively. Therefore, M45 indicates a layer of monosized 0.89-mm spheres closely packed in a triangular pattern, with an intrinsic CA of 45°.

In the present paper, three modes for the droplet interaction with the granular surfaces are observed: a droplet with a stable apparent CA without infiltration (mode I), a droplet with a metastable apparent CA before infiltration (mode II), and immediate infiltration (mode III). Figures 5–7 show the sequences of the three-dimensional views for the representative cases M75, M60, and M30. Supplemental videos are also provided in the Supplemental Material [59]. In addition, Fig. 8 illustrates the temporal evolution of the side projected area A_{proj} of the droplets above the soil surface normalized by the

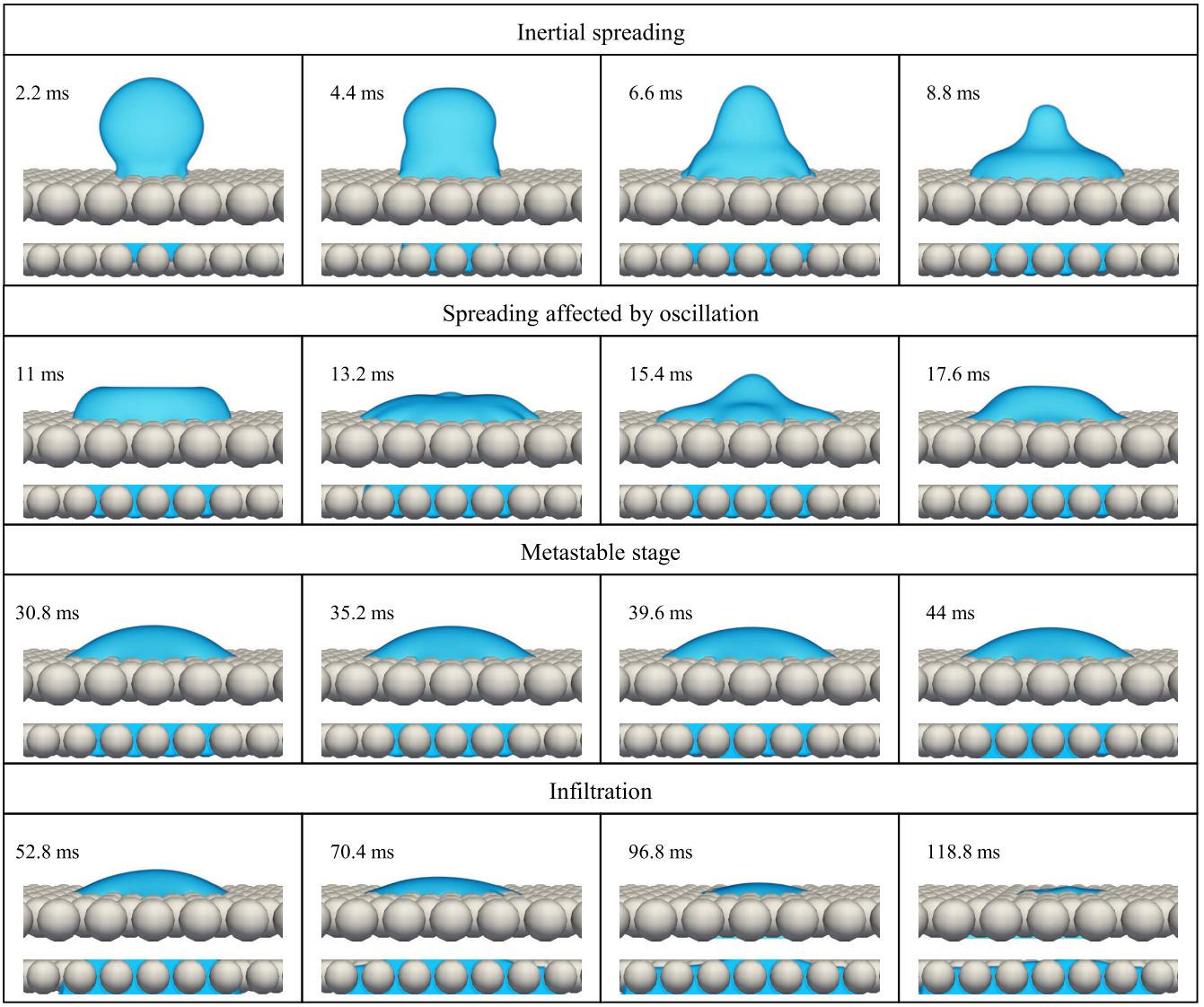

FIG. 6. Typical behavior for mode II: time sequence for test M60 with $D_{\text{particle}}/D_{\text{drop}} = 1:3$; at each time, the upper layer denotes the drop shape and contact line movement and the lower layer denotes the infiltration.

initial projected area A_0 in the three modes. The snapshots indicate that the droplet dynamics is characterized by the coupling between the contact line lateral propagation on the granular surface and the imbibition of the liquid into the porous medium. No splitting or splashing is intended or observed, as in the studies on high-velocity impacts [60,61]. The top views for all the three modes are also provided in Figs. 9–11, which clearly illustrate the droplet infiltration through radial pore-scale flows below the granular surface.

Figure 5 indicates that mode I occurs if the downward breakthrough of the droplet into the pores can be balanced by the upward concave water menisci. After touching the granular surface, the droplet spreads laterally while partially saturating the pores. The contact line crosses the pores before getting pinned to the granular surface. Thereafter, it oscillates and reaches the steady state after the dissipation of the kinematic energy at 125 ms (Fig. 8). Figure 5 shows that a significant portion of the droplet with a spherical-cap shape is maintained above the granular surface, converging to a stable apparent CA. In addition, Fig. 9 shows that the sequence of the top views resembles an evolving circular shape, and the droplet does not infiltrate into the granular surface. Since the pores are partially intruded by the liquid with entrapped air, the final configuration of the droplet on the granular surface can be regarded as a transitional state between Cassie-Baxter and Wenzel.

Mode II in Fig. 6 occurs if the pore throats fail to prevent the droplet infiltration and the imbibition process goes on until fully saturating the pores underneath. At its final state at 118.8 ms, the droplet is entirely absorbed and displays a zero apparent CA. Figure 6 indicates that the droplet maintains the shape of a spherical cap, displaying a slowly evolving apparent CA between 30.8 and 44 ms. In terms of the configuration of the liquid with the granular surface, this stage is consistent with mode I. Figure 10 confirms that the evolution of the droplet during this stage is also very slow when observed from the top view. It is therefore termed as a metastable stage which is unique to mode II. Afterwards, from 44 to 52.8 ms, an acceleration of the imbibition rate is observed. A closer look

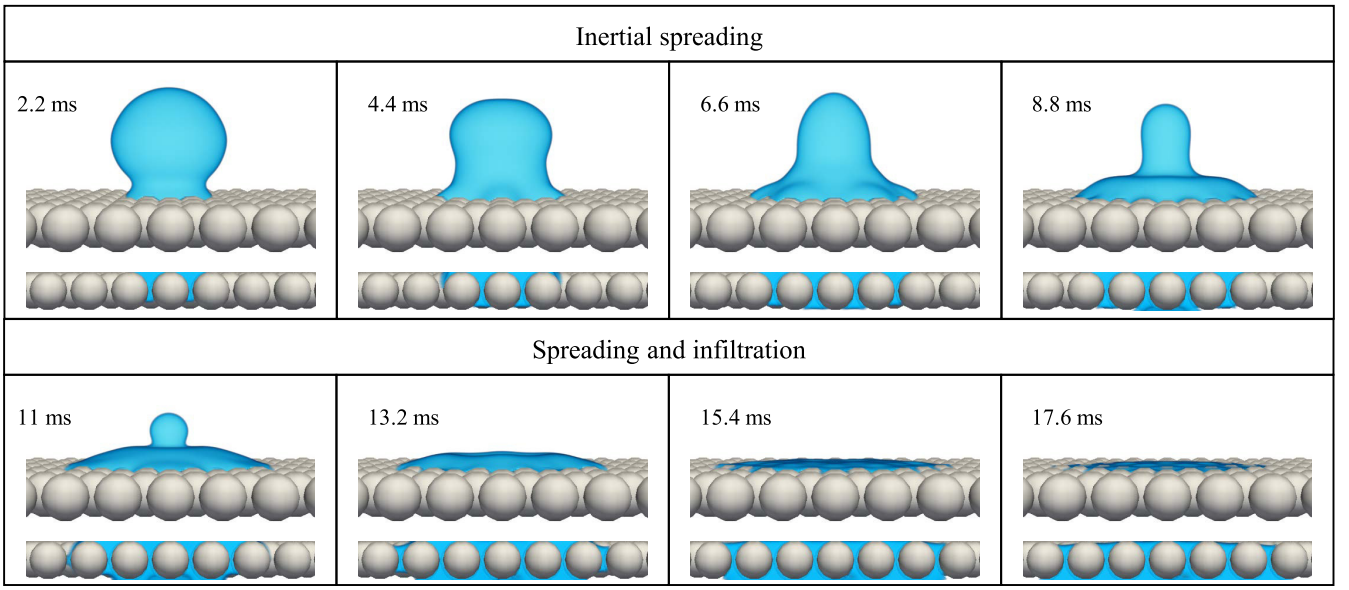

FIG. 7. Typical behavior for mode III: time sequence for test M30 with $D_{\text{particle}}/D_{\text{drop}} = 1:3$; at each time, the upper layer denotes the drop shape and contact line movement and the lower layer the denotes infiltration.

at the flows through the pores sheds light on a highly nonlinear imbibition process. While temporarily supporting the droplet, the pores are getting filled with liquid at a relatively slow rate. However, as some pores are nearly full, at 39.6 ms, the intruding liquid switches to radial flow through the subsurface channels formed between the particles and the base plane. It is the further development of the radial subsurface flow that triggers the speeding up of the infiltration. After 52.8 ms, as Fig. 10 indicates, the radial flow still continues by wetting the pores underneath the granular surface, although the wetted zone above the surface is diminishing with the contact lines of the droplet retreating.

Mode III in Fig. 7 occurs when the infiltration rate is sufficiently high so that the droplet is not allowed to recoil and form the spherical shape before completely infiltrating. The pore-scale flow in Fig. 7 reveals that the horizontal subsurface flow subsequent to the liquid breakthrough into the pores takes place at an early stage, 11 ms in comparison to 39.6 ms for model II. As a result, unlike the significant recoiling and oscillation present in mode I and II, the projected area decreases monotonically with time (Fig. 8), with the infiltration occurring within 15.4 ms. This immediate infiltration is also confirmed in Fig. 11.

B. Phase diagram

A phase diagram is established in Fig. 12 to summarize the modes for each combination of intrinsic CA and particle size. In general, the droplet dynamics changes from mode I to mode III in response to a decreasing intrinsic CA. As for the effect of the particle size, a larger particle favors the transition from mode II to mode III for the same intrinsic CA, while the transition from mode I to mode II is size independent. Three tests at CA $= 65^\circ$ confirmed that the critical intrinsic CA irrespective of particle size is between 60 and 65°.

The transition from mode I to II can be interpreted as the breakdown of the equilibrium state between pairs of surface tensions at the liquid-air, liquid-solid, and solid-air interfaces and gravity under a droplet configuration with partially filled pores. Changing the intrinsic CA is equivalent to modifying

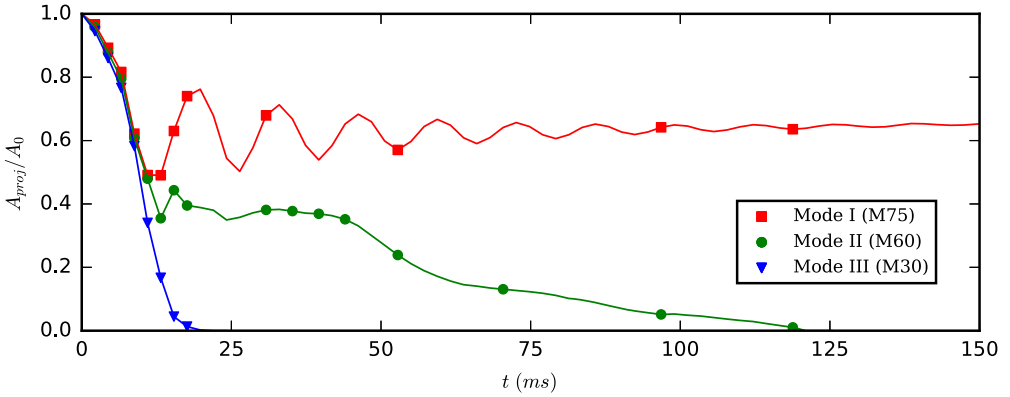

FIG. 8. Normalized projected areas plotted against time for tests M75, M60, and M30, which illustrate the typical behaviors of mode I, II, and III, respectively. The markers refer to instants to take the snapshots shown in Figs. 5–7.

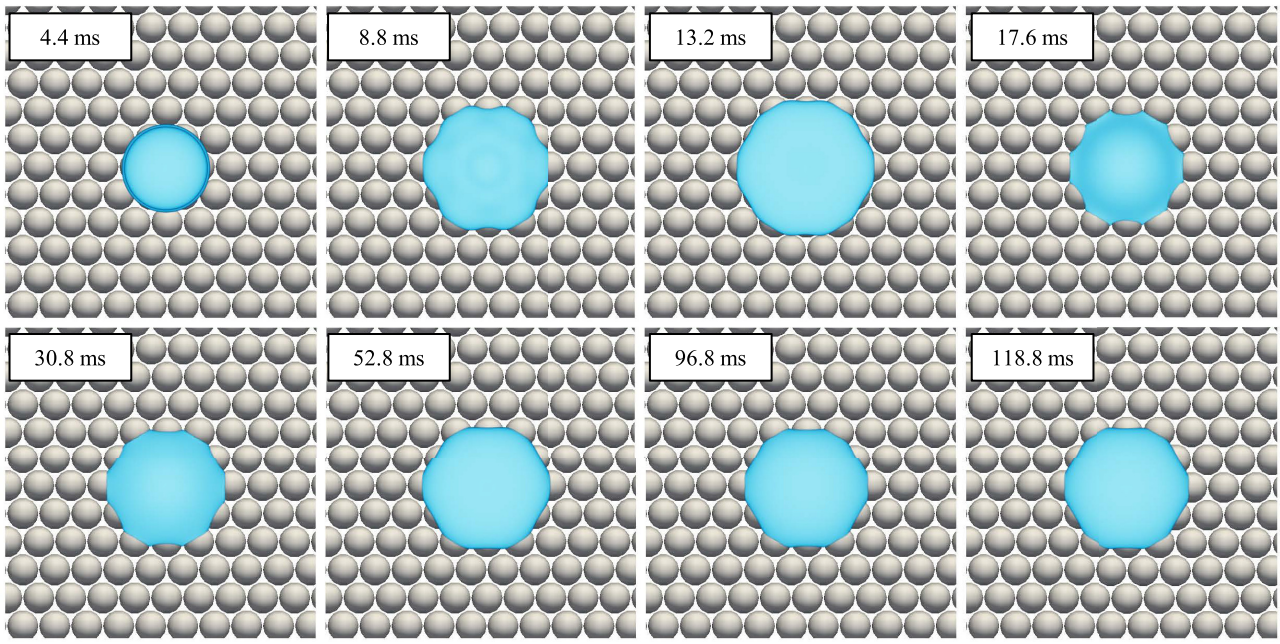

FIG. 9. Top view for mode I: time sequence for test M75 with $D_{\text{particle}}/D_{\text{drop}} = 1:3$.

the difference between the liquid-solid and solid-air surface tensions, which directly affects the location of the water menisci. Further decreasing the intrinsic CA will get the liquid moving downward and propagate laterally through the subsurface pores. That means mode I is no longer a possible configuration for the buildup of forces in equilibrium. As for the effect of the particle size, it is easier for a droplet to percolate into larger pores between larger particles under gravity. However, within the range of the particle sizes in this paper, the length scales of the water menisci bridging the pores in the close triangular packing are smaller than the capillary length (the length scale above which the gravity affects the curvature of an interface) $\lambda_c = \sqrt{\frac{\sigma}{\rho_l g}} = 2.7$ mm. Thus, gravity is a minor factor while the equilibrium among the surface tensions plays a dominant role, which may explain the comparable critical CA between 60 and 65°. This CA value is different from the simulations on a porous surface with perforated tubes, where the liquid infiltrates with an intrinsic CA below 90° [30,31,33]. In our simulations, the smaller critical intrinsic CA can be attributed to the variable pore sizes of the granular surface. The larger pore bodies are connected to each other through smaller pore throats. Due to the ink-bottle effect [62], the menisci downward breakthrough is constrained around the narrow throats even when the intrinsic CA is smaller than 90°.

The boundary separating mode II from mode III reveals a threshold where the downward infiltration outpaces the lateral spreading and prevents the recoiling of the droplet (Figs. 6 and 7). Similar to previous studies on a droplet impacting on a patterned surface [63,64], the two competing processes (downward infiltration versus lateral spreading) evolve in two time scales: one related to the capillary forces during the droplet infiltration normal to the surface, t_1, and the other for the droplet lateral spreading, t_2. Therefore, mode III would require t_1 to be much smaller than t_2, so that the droplet does not have enough time for recoiling into the spherical-cap shape. The time scale t_1 decreases with increasing particle size and decreasing intrinsic CA, both of which favor the downward infiltration as supported by the Washburn equation [16]. With increasing particle size, the metastable stage was shortened for an intrinsic CA = 60° [Fig. 13(b)] and suppressed for an intrinsic CA = 45° [Fig. 13(a)], triggering the transition from phase II to III.

C. Inertial spreading regime

For flat surfaces, the droplet dynamics has been described in three regimes [58]: (1) spreading independent of wettability in which $r \approx t^{0.5}$ within the time $t/\tau_0 \lesssim 0.04$, (2) spreading affected by the surface CA within the time $0.04 \lesssim t/\tau_0 \lesssim (\sigma R/\rho_l v_l^2)^{1/8}$, and (3) slow spreading governed by viscous forces, where τ_0 is the inertial time scale [65]. The first regime is strictly governed by inertia and is characterized by a power law with a constant exponent of 0.5, while the third regime is a slow viscous step with negligible inertial effects. Hence, the second regime is a transitional step influenced by both inertia and viscosity. For low viscous droplets, the second regime is still referred to as the inertial regime, which is also described by a power law [34]:

$$\frac{r}{R} \approx C_0 \left(\frac{t}{\tau_0}\right)^{\alpha}, \tag{18}$$

where α is the power-law exponent and C_0 is the constant. Both coefficients depend on the intrinsic CA. This relationship was further extended to describe the inertial spreading on porous surfaces with perforated tubes [30,33], where both α and C_0 were found to decrease with increasing intrinsic CA and surface porosity.

Here, we attempt to apply the above three regimes to granular surfaces, but are only concerned with the second inertia-dominated regime. The first regime was not observed

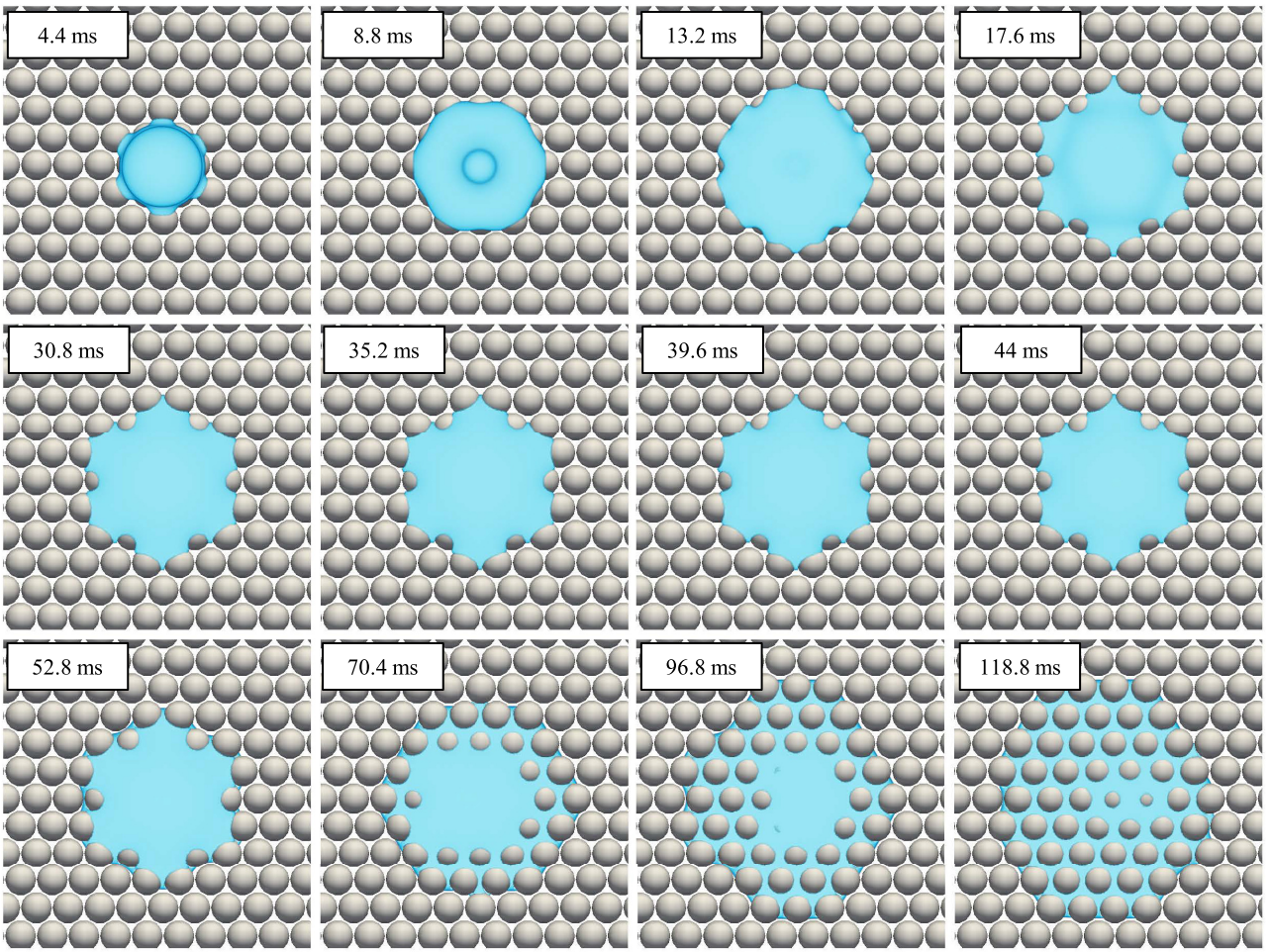

FIG. 10. Top view for mode II: time sequence for test M60 with $D_{\text{particle}}/D_{\text{drop}} = 1:3$.

due to the limited spatial and temporal resolution, and the third regime was not investigated since it was not regarded as a slow viscous spreading step from our simulations in granular surfaces. Instead, the final regime is featured by the droplet oscillation or infiltration.

Figure 14 shows the evolution of the wetted zone radius r normalized by the initial droplet radius R versus the time t normalized by the inertial time scale $\tau_0 = \sqrt{\rho_l R^3/\sigma}$ [65]. The wetted zone expands at an early stage, followed by a receding radius or convergences, depending on whether the droplet will infiltrate or oscillate. The inertial regime indicated by the linear relationship up to $t/\tau_0 \approx 1.8$ depends on the particle size and intrinsic CA of the granular surface. For instance, at $t = 1.8\tau_0$, the normalized wetted zone radius r/R expands to 1.75, 1.68, and 1.51 for S30, M30, and L30, but only 1.36, 1.23, and 1.19 for S105, M105, and L105. The physical time is 10.4 ms, which coincides with the instant the three modes diverge (Fig. 8). Compared to the prediction $(\sigma R/\rho_l v_l^2)^{1/8} = 3.4\tau_0$ for flat surfaces, the duration of $1.8\tau_0$ is shorter. The snapshots at 11 ms in Figs. 5–7 indicate that the liquid infiltration into the pores has already constrained the droplet spreading. Therefore, the inertial regime is

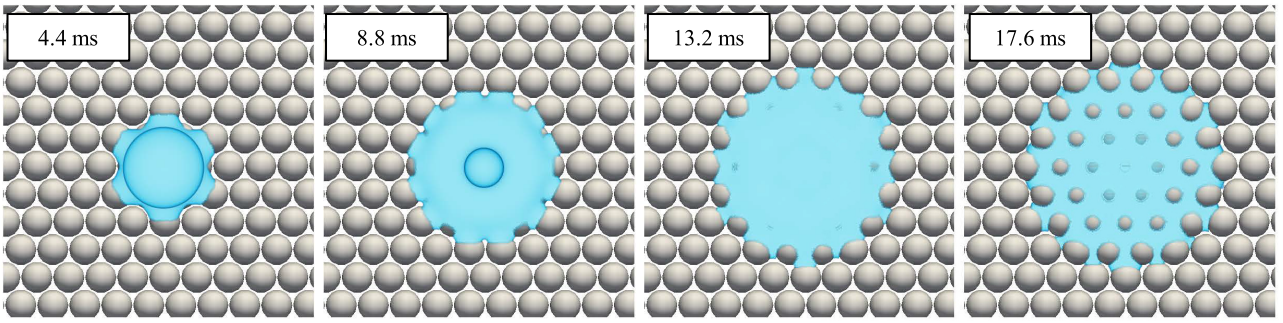

FIG. 11. Top view for mode III: time sequence for test M30 with $D_{\text{particle}}/D_{\text{drop}} = 1:3$.

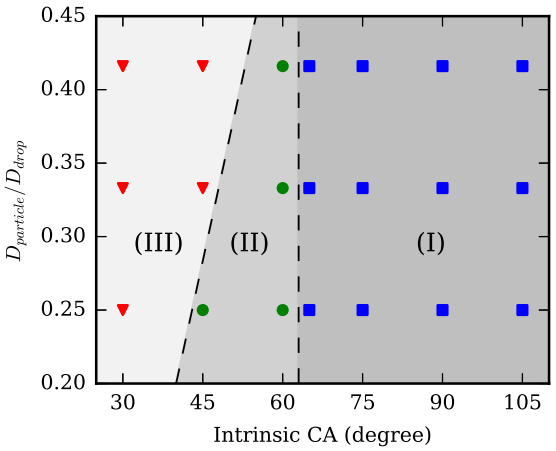

FIG. 12. Phase diagram for different values of intrinsic CA and particle size. Symbols represent interaction modes of droplets with granular surface: mode I, droplet with a stable apparent CA without infiltration (square); mode II, droplet with a metastable apparent CA before infiltration (circle); and mode III, immediate infiltration (triangle).

suppressed, after which droplet dynamics transits to the final regime.

For the inertial regime, the fitted α and C_0 are summarized in Fig. 15. Figure 15(a) shows that C_0 decreases with increasing intrinsic CA, which means that a lower wettability results in a lower driving force of spreading. C_0 also decreases with increasing particle size, since filling larger pores slows down the spreading. The exponent α is around 0.67 as illustrated in Fig. 15(b), and is independent of the particle size and the intrinsic CA. The exponent α reveals the decay on the contact line propagation. In our simulations, the Laplace number is 17 280, indicating that the relative magnitude of viscous forces

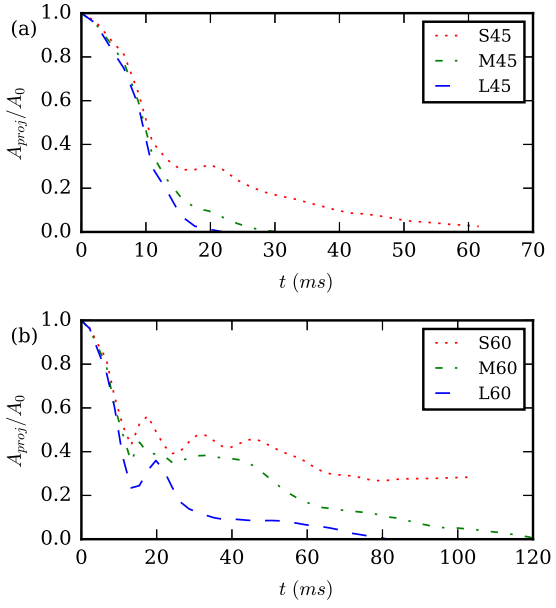

FIG. 13. Normalized projected area as a function of time at different particle sizes for the intrinsic CA equaling (a) 45° and (b) 60°.

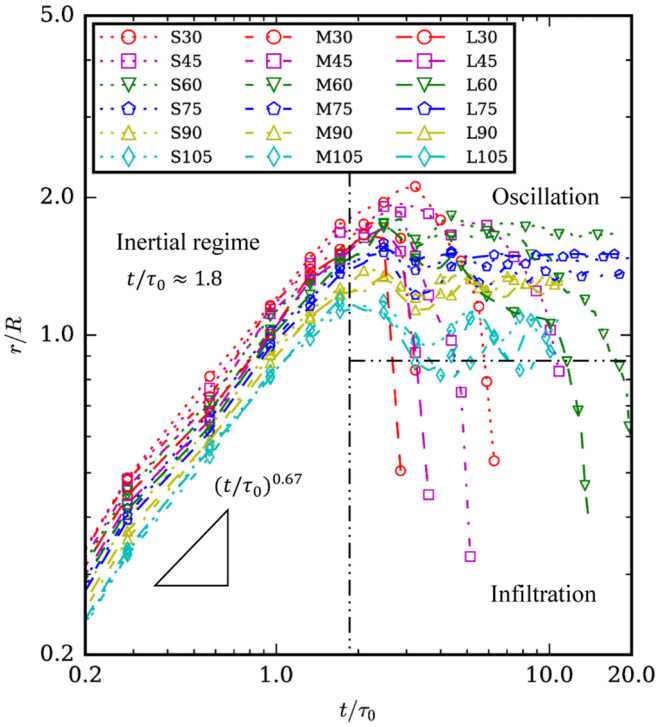

FIG. 14. Normalized wetted zone radius vs dimensionless time.

to inertial and capillary forces is small. Therefore, the viscous forces from the rearrangement of liquid play a minor role, and the generation and propagation of the capillary wave initiated at the contact line comprise the rate limiting process [34].

D. Apparent contact angles

The apparent CA is a measurable property that quantifies the wettability of granular materials. The direct measurement of the apparent CA from Figs. 5–7 provides an opportunity to establish a relation between the apparent CA and the intrinsic CA. Note that the apparent CA can only be analyzed for the droplets in mode I and mode II. For mode I, the reading can be taken after the oscillation stops. For mode II, the apparent CA is measured from the first frame when the droplet displays a spherical-cap shape within the metastable stage [66]. At this instant, the droplet only partially infiltrates into the particle layer and the liquid configuration is consistent with mode I. Since the droplet is not in contact with the bottom plate, the surface wettability of the bottom plate has negligible effects on the apparent CA [12].

Figure 16 shows the apparent CA against the intrinsic CA for the three particle sizes. Despite the scattering due to the discrete nature of particles, the apparent CA increases with the intrinsic CA. A nonzero apparent CA is achieved with intrinsic CAs above 26.2, 37, and 48.8° for the particle sizes 0.67, 0.89, and 1.15 mm, respectively. Since our simulations can capture the transient apparent CA in the metastable stage, those minimum intrinsic CAs are smaller than the 61° predicted by the Bachmann-McHale model. Moreover, the dependence of the apparent CA on the particle size was verified with the apparent CA for larger particles smaller at the low intrinsic CAs. For example, for S60, M60, and L60, the apparent CAs

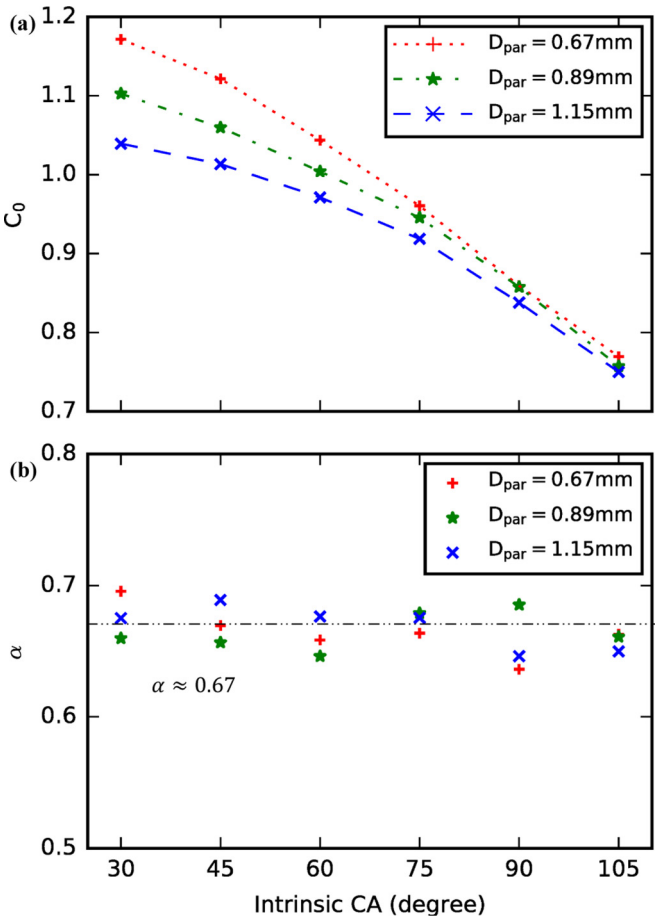

FIG. 15. Coefficients (a) C_0 and (b) α in the power law vs intrinsic CA for various particle sizes.

are 40.2, 37.3, and 21.4° with intrinsic CA = 60°. To explain this, the portion of a droplet embedded into the pores can be interpreted as decreasing the droplet height over the base plane, leading to a lower apparent CA. This justifies the smaller apparent CAs from this research comparing to the Bachmann-McHale model prediction, which takes the embedded volume as infinitesimal relative to the droplet size. For a larger particle, the effect is more significant especially with a low intrinsic CA, since the droplet crosses over more pores and a higher degree of pores is saturated. As the intrinsic CA increases, not only is the location of the contact line residing on the granular surface changing but the less significant embedded volume also contributes to the increase of the apparent CA. At intrinsic CA = 105°, the apparent CAs for S105, M105, and L105 increase to as large as 105.3, 115.6, and 108.8°, respectively.

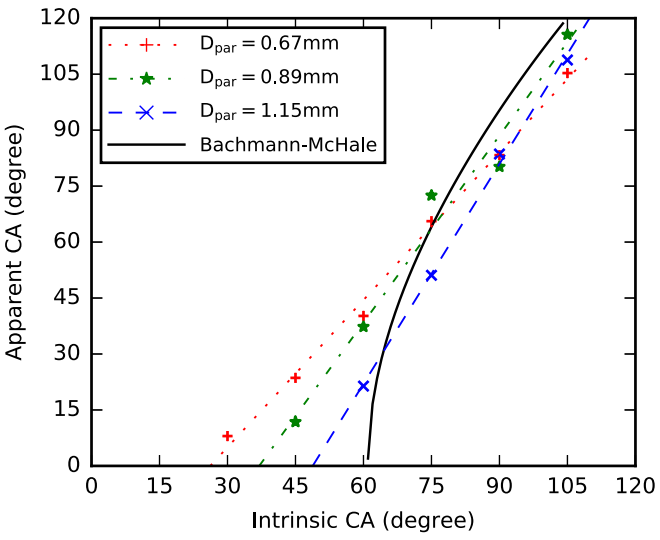

FIG. 16. Apparent CA vs intrinsic CA for various particle sizes.

E. Implications for bulk granular media

The results here obtained are applicable to bulk granular media, such as soils and other granular materials. In this paper, the geometric setup is motivated by the SDM for measuring the apparent CA of granular materials, which involves using a single layer of soil particles attached to a microscope glass slide as the base. The configuration differs from a three-dimensional compacted granular medium, which requires more particle layers. However, compared to multiple layers of particles, using a single layer will not affect the dynamic droplet interaction behavior or the apparent CA for mode I, since the particle layer can support the entire droplet. For mode II, the droplet interaction behavior up to the end of the metastable stage and the corresponding apparent CA are likely not to be affected. For mode III, the apparent CA would always be zero, regardless of the number of layers of particles. Therefore, the apparent CA can be properly measured with a single layer of particles, which has also been experimentally confirmed [12].

The only parameter to be affected by the use of a single layer is the evolution of the projected area A_{proj}/A_0 during infiltration in mode II and mode III. Pore-scale flows will develop in both vertical and radial directions within multiple layers of particles, while for a single-layered sample only the radial flow develops through the subsurface channels formed between the particles and the base plane. Therefore, we assume the infiltration process will be faster with multiple layers of particles.

VI. CONCLUSIONS

The present work investigates a realistic interaction between a millimeter-sized droplet and an idealized granular surface. With the LB method approach, the droplet dynamics can be simulated on a granular surface under various geometric configurations. The particle size, spacing, and shape can be varied to construct different pore structures, which is fundamental to porous media. In this paper, a series of three-dimensional numerical droplet spreading tests were carried out on a granular surface formed by a single layer of spherical particles with different sizes and intrinsic CAs. The droplet dynamics can be described with three modes: a droplet with a stable apparent CA without infiltration, a droplet with a metastable apparent CA before infiltration, and immediate infiltration. The formation of a stable apparent CA requires the complete impedance of the downward liquid infiltration, which only relies on a sufficiently large intrinsic CA. In contrast, the critical configuration to display a metastable apparent CA depends on both intrinsic CA and particle size. Either the increase in the

particle size or the decrease in the intrinsic CA will accelerate the downward infiltration, preventing the formation of the metastable apparent CA. The wetted zone radius expansion during the early stage of spreading was found to be governed by inertia and gravity, which can be characterized by a power law. Finally, the apparent CA revealed a more realistic droplet configuration compared with size-independent models, such as Cassie-Baxter and Bachmann-McHale. The apparent CA for a larger particle is generally smaller in the low CA region but increases faster with increasing intrinsic CA due to part of the volume of the droplet being embedded into the granular surface. Despite the focus on the hydraulic behavior, the implemented LB method approach is also applicable to modeling various dynamic processes that occur in nature, such as evaporation, high-velocity impacting, and lateral sliding in granular materials. The current paper provides a basis to investigate the behavior of droplets in those scenarios.

ACKNOWLEDGMENTS

Financial support provided by the General Research Fund, Research Grants Council, Hong Kong (Grants No. 17221016 and No. 17203417) and the Hong Kong University (HKU) Seed Funding Programme for Basic Research (Grant No. 201406159004) is acknowledged. The computations were performed using research computing facilities offered by Information Technology Services, the University of Hong Kong.

[1] C. Lee, H.-J. Yang, T. S. Yun, Y. Choi, and S. Yang, Vadose Zone J. **14** (2015).
[2] D. Zerihun, C. Sanchez, and A. Warrick, J. Irrig. Drain. Eng. **142**, 04016007 (2016).
[3] S. Ahn, S. H. Doerr, P. Douglas, R. Bryant, C. A. Hamlett, G. McHale, M. I. Newton, and N. J. Shirtcliffe, Earth Surf. Processes Landforms **38**, 1225 (2013).
[4] G. McHale, N. Shirtcliffe, M. Newton, and F. B. Pyatt, Hydrol. Process. **21**, 2229 (2007).
[5] G. Zhang, R. Parwani, C. A. Stone, A. H. Barber, and L. Botto, Langmuir **33**, 12072 (2017).
[6] W. Yang and J. Xu, Colloids Surf. A **516**, 9 (2017).
[7] A. Määttänen, P. Ihalainen, R. Bollström, M. Toivakka, and J. Peltonen, Colloids Surf. A **367**, 76 (2010).
[8] H. Haidara, B. Lebeau, C. Grzelakowski, L. Vonna, F. Biguenet, and L. Vidal, Langmuir **24**, 4209 (2008).
[9] L. Jing, C. Y. Kwok, Y. F. Leung, and Y. D. Sobral, Phys. Rev. E **94**, 052901 (2016).
[10] C. A. Hamlett, N. J. Shirtcliffe, G. McHale, S. Ahn, R. Bryant, S. H. Doerr, and M. I. Newton, Environ. Sci. Technol. **45**, 9666 (2011).
[11] W. Zhang, M. Wahlgren, and B. Sivik, Desalination **72**, 263 (1989).
[12] J. Bachmann, A. Ellies, and K. Hartge, J. Hydrol. **231**, 66 (2000).
[13] W. J. Likos and N. Lu, J. Eng. Mech. **130**, 646 (2004).
[14] V. Richefeu, F. Radjai, and J.-Y. Delenne, Comput. Geotech. **80**, 353 (2016).
[15] L. Hao and P. Cheng, J. Power Sources **195**, 3870 (2010).
[16] E. W. Washburn, Phys. Rev. **17**, 273 (1921).
[17] R. N. Wenzel, Ind. Eng. Chem. **28**, 988 (1936).
[18] A. Cassie and S. Baxter, Trans. Faraday Soc. **40**, 546 (1944).
[19] J. Bachmann and G. McHale, Eur. J. Soil Sci. **60**, 420 (2009).
[20] R. Crawford, L. K. Koopal, and J. Ralston, Colloids Surf. **27**, 57 (1987).
[21] J. Bachmann, S. K. Woche, M.-O. Goebel, M. B. Kirkham, and R. Horton, Water Resour. Res. **39**, 1353 (2003).
[22] T. Dang-Vu, J. Hupka, and J. Drzymala, Physicochem. Probl. Mineral Process. **40**, 45 (2006).
[23] S. Davis and L. Hocking, Phys. Fluids **11**, 48 (1999).
[24] S. Davis and L. Hocking, Phys. Fluids **12**, 1646 (2000).
[25] A. Clarke, T. Blake, K. Carruthers, and A. Woodward, Langmuir **18**, 2980 (2002).
[26] V. Starov, S. Zhdanov, and M. Velarde, Langmuir **18**, 9744 (2002).
[27] L. Espín and S. Kumar, J. Fluid Mech. **784**, 465 (2015).
[28] D. Seveno, V. Ledauphin, G. Martic, M. Voué, and J. De Coninck, Langmuir **18**, 7496 (2002).
[29] J. Hyväluoma, P. Raiskinmäki, A. Jäsberg, A. Koponen, M. Kataja, and J. Timonen, Phys. Rev. E **73**, 036705 (2006).
[30] X. Frank and P. Perre, Phys. Fluids **24**, 042101 (2012).
[31] H. Ding and T. Theofanous, J. Fluid Mech. **691**, 546 (2012).
[32] M. Taghilou and M. H. Rahimian, Comput. Math. Appl. **67**, 424 (2014).
[33] X. Frank, P. Perré, and H.-Z. Li, Phys. Rev. E **91**, 052405 (2015).
[34] J. C. Bird, S. Mandre, and H. A. Stone, Phys. Rev. Lett. **100**, 234501 (2008).
[35] M. Hodson, J. Clim. Appl. Meteorol. **25**, 1070 (1986).
[36] Y. Saulick, S. Lourenço, and B. Baudet, Soil Sci. Soc. Am. J. **81**, 241 (2017).
[37] X. Shan and H. Chen, Phys. Rev. E **47**, 1815 (1993).
[38] X. He, S. Chen, and R. Zhang, J. Comput. Phys. **152**, 642 (1999).
[39] M. R. Swift, W. R. Osborn, and J. M. Yeomans, Phys. Rev. Lett. **75**, 830 (1995).
[40] M. R. Swift, W. R. Osborn, E. Orlandini, and J. M. Yeomans, Phys. Rev. E **54**, 5041 (1996).
[41] T. Inamuro, T. Ogata, S. Tajima, and N. Konishi, J. Comput. Phys. **198**, 628 (2004).
[42] T. Lee and C.-L. Lin, J. Comput. Phys. **206**, 16 (2005).
[43] T. Lee and L. Liu, J. Comput. Phys. **229**, 8045 (2010).
[44] S. Succi, E. Foti, and F. Higuera, Europhys. Lett. **10**, 433 (1989).
[45] L. Hao and P. Cheng, Int. J. Heat Mass Transf. **53**, 1908 (2010).
[46] C. Pan, M. Hilpert, and C. T. Miller, Water Resour. Res. **40**, W01501 (2004).
[47] M. E. A. B. Amara, P. Perre, and S. B. Nasrallah, J. Porous Media **19**, 453 (2016).
[48] F. Jansen and J. Harting, Phys. Rev. E **83**, 046707 (2011).
[49] M. Cates, K. Stratford, R. Adhikari, P. Stansell, J. Desplat, I. Pagonabarraga, and A. Wagner, J. Phys.: Condens. Matter **16**, S3903 (2004).

[50] T. Lee and L. Liu, Phys. Rev. E **78**, 017702 (2008).
[51] K. Connington and T. Lee, J. Mech. Sci. Technol. **26**, 3857 (2012).
[52] H. Chen, S. Chen, and W. H. Matthaeus, Phys. Rev. A **45**, R5339 (1992).
[53] H. Huang, M. Sukop, and X. Lu, *Multiphase Lattice Boltzmann Methods: Theory and Application* (Wiley, New York, 2015).
[54] Y. Wang, C. Shu, H. Huang, and C. Teo, J. Comput. Phys. **280**, 404 (2015).
[55] X. Shan, Phys. Rev. E **73**, 047701 (2006).
[56] J. D. Anderson and J. Wendt, *Computational Fluid Dynamics* (Springer, New York, 1995), Vol. 206.
[57] S. H. Y. Ng and S. D. N. Lourenço, Géotechnique **66**, 441 (2016).
[58] K. G. Winkels, J. H. Weijs, A. Eddi, and J. H. Snoeijer, Phys. Rev. E **85**, 055301 (2012).
[59] See Supplemental Material at http://link.aps.org/supplemental/10.1103/PhysRevE.98.012902 for videos of the various modes of droplet dynamics.
[60] M. Reyssat, F. Pardo, and D. Quéré, Europhys. Lett. **87**, 36003 (2009).
[61] M. Reyssat, D. Richard, C. Clanet, and D. Quéré, Faraday Discuss. **146**, 19 (2010).
[62] L. Sarkisov and P. Monson, Langmuir **17**, 7600 (2001).
[63] Y. Liu, L. Moevius, X. Xu, T. Qian, J. M. Yeomans, and Z. Wang, Nat. Phys. **10**, 515 (2014).
[64] L. Moevius, Y. Liu, Z. Wang, and J. M. Yeomans, Langmuir **30**, 13021 (2014).
[65] A.-L. Biance, C. Clanet, and D. Quéré, Phys. Rev. E **69**, 016301 (2004).
[66] A. F. Stalder, T. Melchior, M. Müller, D. Sage, T. Blu, and M. Unser, Colloids Surf. A **364**, 72 (2010).